JOURNAL OF MATERIALS RESEARCH AND TECHNOLOGY 2023;22:1855–1867

Available online at www.sciencedirect.com

jmr&t Journal of Materials Research and Technology

journal homepage: www.elsevier.com/locate/jmrt

Original Article

Self-activating metal-polymer composites for the straightforward selective metallization of 3D printedparts

Caterina Credi [a,b,*,†], Roberto Bernasconi [c,†], Marinella Levi [d], Luca Magagnin [c]

[a] Istituto Nazionale di Ottica, Consiglio Nazionale delle Ricerche (INO-CNR), Via Madonna del Piano 10, 50019, Sesto Fiorentino, Italy

[b] LENS - European Laboratory for Non-Linear Spectroscopy, Via Nello Carrara 1, 50019, Sesto Fiorentino, Italy

[c] Dipartimento di Chimica, Materiali e Ingegneria Chimica "Giulio Natta", Politecnico di Milano, Via Mancinelli 7, 20131, Milano, Italy

[d] Dipartimento di Chimica, Materiali e Ingegneria Chimica "Giulio Natta", Politecnico di Milano, Piazza Leonardo da Vinci 32, 20133, Milano, Italy

ARTICLE INFO

Article history:
Received 19 May 2022
Accepted 6 December 2022
Available online 10 December 2022

Keywords:
Stereolithography
Composite
Nickel
Electroless plating
Selective metallization

ABSTRACT

The integration of multifunctional elements directly embedded in three-dimensional (3D) printed parts is the cutting-edge of additive manufacturing (AM) and it is crucial for enlarging as well as for strengthening AM role in industrial applications. Here, a straightforward and low-cost method that synergically combines stereolithography (SLA) and selective electroless metallization (EM) is presented for the fabrication of 3D parts characterized by complex shapes and end-use multifunctionalities (conductive, magnetic, mechanical properties). To this end, a novel photocurable composite based on acrylate resin loaded with nickel (Ni) particles is developed for high-resolution SLA-printing of features with self-catalytic properties for EM. Ni particles are loaded in the resin to trigger metal deposition avoiding time consuming and expensive laser-based surface activation. The effect of Ni content on SLA behavior as well as on the efficiency of EM process is studied. Metallized SLA cured samples show good electrical and magnetic properties as well as improved robustness with respect to their non-loaded counterparts. Then, selective metallization of 3D printed parts is successfully achieved by implementing a multi-material SLA-printing where loaded and non-loaded resins are properly interchanged with strong adhesion at the interface, thus offering a cost-effective approach for rapid prototyping of functional free-form features on 3D structures.

* Corresponding author.
E-mail address: caterina.credi@ino.cnr.it (C. Credi).
† Equal contribution of the authors.

https://doi.org/10.1016/j.jmrt.2022.12.035

1. Introduction

To date, additive manufacturing (AM) or three-dimensional (3D) rapid prototyping technologies are widely recognized as powerful technologies enabling to fabricate complex 3D objects of virtually any shape with time, material, and cost-saving processes. Intricate physical parts can be directly built up in a layer-by-layer fashion by spatially controlled deposition of materials, where each layer represents a thin cross-section of the part derived from computer-aided designed (CAD) files [1,2], avoiding extra-costs generally needed in conventional manufacturing for assembling tools and surface finishing as well [3]. Indeed, the portfolio of 3D printing processes includes well-established technologies guaranteeing high design flexibility of structures at the micrometric scale with printing resolution ranging from 150 μm for fused deposition modeling (FDM) fabrication down to 10 μm for stereolithography (SLA). Furthermore, a huge research effort has been made in materials science and engineering to develop novel 3D printable materials characterized by improved properties and, among all, by new functionalities, such as magnetic properties [4] and conductive properties [5–7]. To this end, the gold strategy relies on doping polymeric matrices with nanoparticles or fibers [8,9] thus obtaining thermoplastic or photo-curable composites, FDM- or SLA-printable, respectively. This approach opened concrete perspectives for the straightforward fabrication of geometrically complex objects with embedded functional parts and, for instance, it has already been explored for 3D printing of lightweight and compact electronics systems [10,11]. The functionalities of the resulting composites can be further enhanced by properly selecting 3D printing conditions in order to align and organize the fillers present in the material [12,13]. Many of the examples reported use FDM technology, but research is also focusing on other 3D printing approaches, like direct ink writing (DIW) [14] or SLA [15,16], for the additive manufacturing of functional polymeric composites. SLA in particular, due to its high resolution, could potentially enable to further reduce the footprint of finished parts [17,18] and overcome the intrinsic limitations of FDM processes.

Furthermore, metal containing SLA composites can be exploited for their magnetic/conductive properties or for their mechanical behavior but also for their potential capability to trigger selective electroless deposition. The latter requires the presence of a catalytic surface [19], which is constituted by the metallic particles embedded in the SLA printed composite. This approach can enable the 3D printing of self-metallizing parts. Furthermore, selective metallization can be easily achieved by fabricating parts in a multi-material printing process [20] with both metal loaded and non-loaded resins. Since only the layers that contain the catalyzing deposition particles can metallize, conductive regions can be alternated with insulating zones to create metallic functional patterns on the surface of complex SLA printed parts. This kind of approach may find applicability in the production of flexible and highly 3D electronic circuits [21], radiofrequency devices [22], microelectromechanical systems [23] and microfluidic setups [24].

The importance of selective wet metallization over polymeric 3D printed parts is demonstrated by the wealth of different strategies developed in the last few years. Indeed, while the electroless metallization of 3D printed parts is relatively easy [25,26], patterning only specific areas with the metal presents relevant challenges. In the case of polymers, the catalytic surface required to start the plating reaction is obtained by depositing nanoclusters of noble metals, which are normally indiscriminately applied by immersion. Some selective metallization methodologies work on this aspect by patterning the catalyst on the surface. Li et al. [27], for example, exploited a non-platable polymer in combination with a platable one to guide the absorption of a palladium/tin colloidal catalyst on the surface of FDM printed parts. Chen et al. [28] applied *via* inkjet printing a silver ink on the surface of a 3D printed part to trigger Cu electroless deposition. Ryspayeva et al. [29] employed a photomask to pattern Ag nanoparticles able to start electroless Cu deposition. Another interesting approach can be the inclusion of a metal precursor in the resin, which is converted into the active metal by selective exposure to a laser beam. This is the approach followed by Zhang et al. [21,30], Xu et al. [31], Rytlewski et al. [32], Li et al. [33], Lee et al. [34] and Taormina et al. [35]. Following other approaches, Ha et al. [36] employed a selective functionalization approach to fabricate metal-polymer microhybrids, while Jammes et al. [37] simply selectively sprayed Ag on 3D printed parts. The last promising approach to implement selective metallization can be the direct inclusion of the catalyst in the 3D printable polymer. This strategy has been demonstrated viable for DIW [38] and FDM [39,40].

The main aim of the present work is the development of a SLA printable composite based on acrylate resin loaded with Ni particles and its application as self-catalytic material for electroless metallization. Indeed, by directly including the catalytic Ni particles in the polymer, the electroless deposition process can be triggered without the need to activate the surface of the SLA printed parts. With respect to reported examples, this approach, unprecedented for SLA resins, eliminates the need of noble metal activation of the surface that relies on expensive and time-consuming laser-based steps. Moreover, the usage of Ni is of great interest also due to the other properties that it can potentially impart to the printed parts: improved mechanical properties, high thermal conductivity [41], magnetizability [42]. In the first part of the work, following Jacobs theory [43], the SLA printability of the novel metal-loaded resin was assessed by quantifying the critical energy E_c and the penetration depth D_p of the formulation; defined respectively as the dose of energy required to cross-link the resin and the penetration of the laser within it. Consequently, to achieve better printing resolution of built objects, novel SLA formulations are developed to minimize the penetration depth thus confining the laser radiation and curing thinner layers of materials that are stacked together. Instead, small E_c values enable fast polymerization and speed up the printing process. D_p end E_c values reported from the literature for commercially available SLA-processable formulations are considered as benchmark values [44,45]. Then, the structural properties of the 3D printed composites were investigated. The morphology was studied using scanning electron microscopy (SEM), while the phase composition was analyzed by means of X-rays diffraction (XRD). Subsequently, the functional properties of the composites were determined,

placing a particular emphasis on their capability to trigger NiP electroless deposition. Their magnetic behavior was studied using vibrating sample magnetometry (VSM) and the elastic modulus of the composites was determined via Vickers microindentation. Finally, the possibility to selectively metallize only desired areas of the 3D printed parts was successfully demonstrated by metallizing a Ni-loaded pattern that was 3D printed on a Ni-free base exploiting multimaterial SLA printing.

2. Experimental section

2.1. Raw materials and resin formulations

Bisphenol A ethoxylate diacrylate (SR349, density 1.146 g/mL, viscosity 1500–2000 mPa s at 25 °C), the photoinitiator (PI) 2,4,6-trimethylbenzoylphenyl phosphinate (Irgacure TPO-L, indicated as TPO-L here on) and Ni nanopowder (≥99% trace metals basis) were purchased from Merck. Photopolymerizable mixtures were obtained by mixing SR349 with the TPO-L at 4 % wt. under magnetic stirring at room temperature for 30 min. Based on previous extensive studies from our group, the PI content was selected to decrease the printing resolution [45]. Then, Ni nanoparticles were added to the SR349 system at 30 % wt. and 50% wt. with respect to the weight of the photopolymer SR349. To achieve homogeneous nickel dispersion, the formulation was stirred for 4 h at 350 rpm and then ultrasonicated for 30 min with a sonicator tip. This last step was carried out in an ice bath to prevent undesired exothermic phenomena resulting from the ultrasonication process and possibly affecting the photocurable efficiency.

2.2. SLA printing tests

To determine the printability window of Ni-doped SR349 systems at different loading percentages, a "wedgeplot" method derived from the standardized diagnostic WINDOWPANE™ technique [3,43] was exploited to determine the critical energy E_c and the sensitivity D_p of the formulations. E_c and D_p are purely resin parameters used to describe the SLA behavior of formulations and are defined as the dose of energy required to crosslink the liquid resin and the laser penetration within it, respectively. A bench top DWS XFAB2500 HD stereolithography (Digital Wax Systems, Italy) was used. The SLA-apparatus is equipped with a monochromatic actinic laser source (Solid State Bluedge® BE-1500A/BE-1500AHR) with an emitting output power of 30 mW at $\lambda = 405$ nm and 50 μm laser spot diameter. During the wedgeplot experiment, the laser is scanned across the photopolymer surface by galvo-scanner to draw five rectangles (10 × 20 mm) with tuned laser velocity, thus resulting in different energy doses and consequently in different samples thicknesses (C_d). The average energy exposure E_{av} (mJ/cm^2) was calculated according to:

$$E_{av} = P_L / V_s h_s \quad (1)$$

where P_L is the laser power (mW), h_s is the laser line spacing (0.02 mm), and V_s is the laser scanning speed which was varied in the range 50–2000 mm/s (standard laser window working conditions for the DWS XFAB-2500hD printer) through Fictor® SLA fabrication dedicated software. Polymerized wedgeplots were rinsed with ethanol to remove unreacted resin and the cured thickness C_d was measured with a micrometer on 4 different areas of the samples. Each composition was measured twice. Following the Jacob's relationship, here reported as Eq. (2), the measured cure depths can be plotted against the logarithm of average energy doses giving a straight line, known as the "working curve", whose slope represents the penetration depth D_p and the x-intercept is the critical energy E_c, both independent of laser power.

$$C_d = D_p \ln(E_{av} / E_c) \quad (2)$$

Test samples, which were used for the characterization and for the metallization tests, were printed using the nanocomposite formulations at 10 % wt., 30 % wt. and 50 % wt. Ni in combination with the optimal printing parameters determined from the laser working curves.

The 30 % wt. Ni formulation was also exploited for 3D printing of multimaterial compact rectangular-shaped demonstrators. These were constituted of a square clear resin base supporting Ni-doped structures that were designed using "Solidworks" software (Dassault Systemes, France). As a proof-of-concept, an intricate linear path with squared cross section was designed (Fig. S1). Then, the CAD model was processed with Nauta® and sent to Fictor®, the proprietary DWS software that directly controls the 3D printer and performs the slicing operation according to the user-imposed building parameters. Based on D_p and E_c values previously measured that identifies the printability window, the SR349 part was built with laser speed ranging between 500 and 5000 mm/s and layer thickness between 10 and 50 μm while the Ni-doped SR349 part was all built at 200 mm/s laser speed with 15 μm layer fixed layer thickness. Multimaterial SLA process was successfully obtained by pausing the printing process at the desired slice, switching the formulations in the machine vat and restarting the procedure until the object is finalized. At the end, the objects are released from the building platform and washed twice with ethanol to remove unreacted resin and dried with nitrogen. To accomplish photopolymer conversion, the SLA-printed objects were further exposed to light for 30 min in a dedicated UV-curing unit ($\lambda = 405$ nm, Digital Wax Systems).

2.3. Composites metallization

3D printed and postcured samples were initially degreased in ethanol under sonication. Their surface was then etched in KOH 200 g/l for 30 min at 45 °C. Ni oxide or hydroxyde eventually present on the surface of the Ni nanoparticles at the end of the etching step was removal immersing the samples in 3.2 % wt. HCl for 1 min. After this stage, samples were immediately immersed in the NiP electroless bath for 20 min at 45 °C. 3D printed parts were carefully washed with deionized water after each step. The composition of the electroless bath was the following: 32 g L^{-1} $NiSO_4 \cdot 6H_2O$, 20 g L^{-1} $Na_3C_6H_5O_7$, 25 g L^{-1} NH_4Cl and 28 g L^{-1} $NaH_2PO_2 \cdot H_2O$. The pH was corrected to 9 using an aqueous solution of NH_4OH. The deposition was performed under vigorous stirring at 45 °C.

2.4. Samples characterization

Thermogravimetric analyses (TGA) were carried out with a Q500 (TA Instrument) to determine the effective content of Ni nanoparticles loaded within the polymer matrix. Non isothermal experiments were performed on postcured samples loaded with different percentages of nanoparticles in the temperature range 25–900 °C at a 10 °C/min heating rate under nitrogen. The differential scanning calorimetry (DSC) analysis was performed with a STARe SW9:30 instrument by Mettler Toledo in order to determine the thermal properties of both Ni-loaded and unloaded samples. XRD was carried out to determine the phase composition of the composites using a Philips XpertMPD with $Cu_{K\alpha}$ = 1.5406 Å. Scanning electron microscopy (SEM, Carl Zeiss EVO 50 Extended Pressure microscope) and energy dispersive X-rays analyses (EDS, model 7060 module from Oxford Instruments) were performed on 3D printed devices to evaluate the nanoparticles dispersion, the thickness and the morphology of the deposited metal layer.

2.5. Data repeatability

The experiments and the characterization tests were repeated at least two times, in most cases three times, to evaluate repeatability. No significant deviations from the data presented were observed.

3. Results and discussion

3.1. Resin formulation and SLA printing tests

The straightforward approach we present to 3D print multifunctional parts embedded in structural parts by stereolithography is depicted in the scheme in Fig. 1. With respect to the methods reported from the literature [33,34], the novel metal-polymer composite hereby described, enables direct 3D printing of self-activating structures that can be selectively metallized *via* electroless processes, avoiding time consuming and expensive intermediate processes generally required between the 3D printing and electroless deposition steps for surfaces activation through laser pattern irradiation.

The key point to be addressed was the formulation of self-catalyzing photopolymers optimized for high-resolution 3D printing by means of stereolithography. To this end, the acrylate-based SR349 resin was doped with Ni particles that can trigger the electroless deposition process avoiding the post-printing selective activation of the surfaces of the printed parts. The main challenge was to achieve a homogeneous dispersion of the catalyst within the highly viscous polymer matrix while guaranteeing optimal stereolithographic behavior in terms of SLA-laser printability. According to previous results from our group [45], the starting mixture was obtained by mixing the neat resin with TPO-L photoinitiator at 4% wt. Then, Ni was added at increasing concentration till 50% wt. As shown in the OM images reported in Fig. 2a, macroscopic homogeneous dispersion was obtained by shear mechanical stirring for all the Ni loading investigated. The stereolithographic behavior parameters D_p and E_c for the Ni-doped mixtures were determined experimentally and compared with parameters of the commercial high-performing SLA resin which were taken as benchmark (D_p = 0.079 mm and E_c = 9.5 mJ/cm^2). According to the Jacob's equation, D_p and E_c were the slope, and the intercept of the laser working curves obtained by linearly fitting the experimental WINDOWPANE data (Fig. 2b). As expected, a strong effect on resin sensitivity was observed with D_p values decreasing from 0.28 mm till 0.028 mm upon increasing with Ni content. This is likely due to the absorption and scattering phenomena by the particles that reduce the laser penetration into the polymer matrix thus resulting in higher vertical resolution. No significant trend was observed for the E_c values which varied within 2–6 mJ/cm^2, largely included in the range typically measured for the acrylate-based formulations developed for SLA processing (Fig. 2c).

3.2. Composites characterization

At the end of the SLA optimization process, test samples at different Ni content were printed and characterized to assess their morphology as well as their mechanical and magnetic properties. SEM images were acquired for samples with Ni content higher than 10 % wt. (considered more interesting for their functional properties) are reported in Fig. 3a and b. The secondary electrons (SE) signal was exploited. The morphology of a cured Ni-free SR349 resin sample was also acquired for comparison (Fig. S2). If compared to the SEM image of their non-loaded counterpart (Fig. S2), Ni loaded samples clearly evidenced a rougher morphology. In general, Ni-free SR349 was characterized by a relatively flat appearance, which translated into a value of R_a equal to 166 nm. The surfaces of the two samples containing Ni nanoparticles, on the contrary, were characterized by pronounced asperities (Fig. 3a and b). Indeed, the R_a values measured in these two cases were significantly higher (445 ± 55 nm for the 30% wt. Ni sample and 451 ± 49 nm for the 50% wt. Ni sample). As expected, the presence of a large quantity of Ni nanoparticles is evident in both the samples with relatively homogeneous dispersion and with not significant accumulation in preferential areas of the samples. Ni was more evident by exploiting the backscattered (BS) electrons signal, which is highly sensitive to the atomic weight of the elements present. Consequently, as shown in Fig. 3c, Ni nanoparticles appeared white due to the large atomic weight difference with the carbon-rich SR349 resin. The high contrast obtained from the BS electrons allowed to determine the mean diameter of the particles, which resulted equal to 992 ± 317 nm. The large standard deviation obtained was a direct consequence of the high variability observed in the diameters of the particles.

The TGA curves obtained for the Ni loaded resins at different percentages (10 % wt., 30 % wt. and 50 % wt. Ni) are reported in Fig. 4a. All the curves show a first mass loss step within the range of 200–250 °C which can be likely due to unreacted monomer or photoinitiator fragment degradation. The main step loss corresponding to SR349 matrix degradation started immediately after and the material totally burned between 400 and 460 °C. From the derivative TGA graph reported in Fig. S3, it is evident that the polymer matrix degradation temperature slightly decreases while increasing in Ni content thus indicating higher thermal stability for

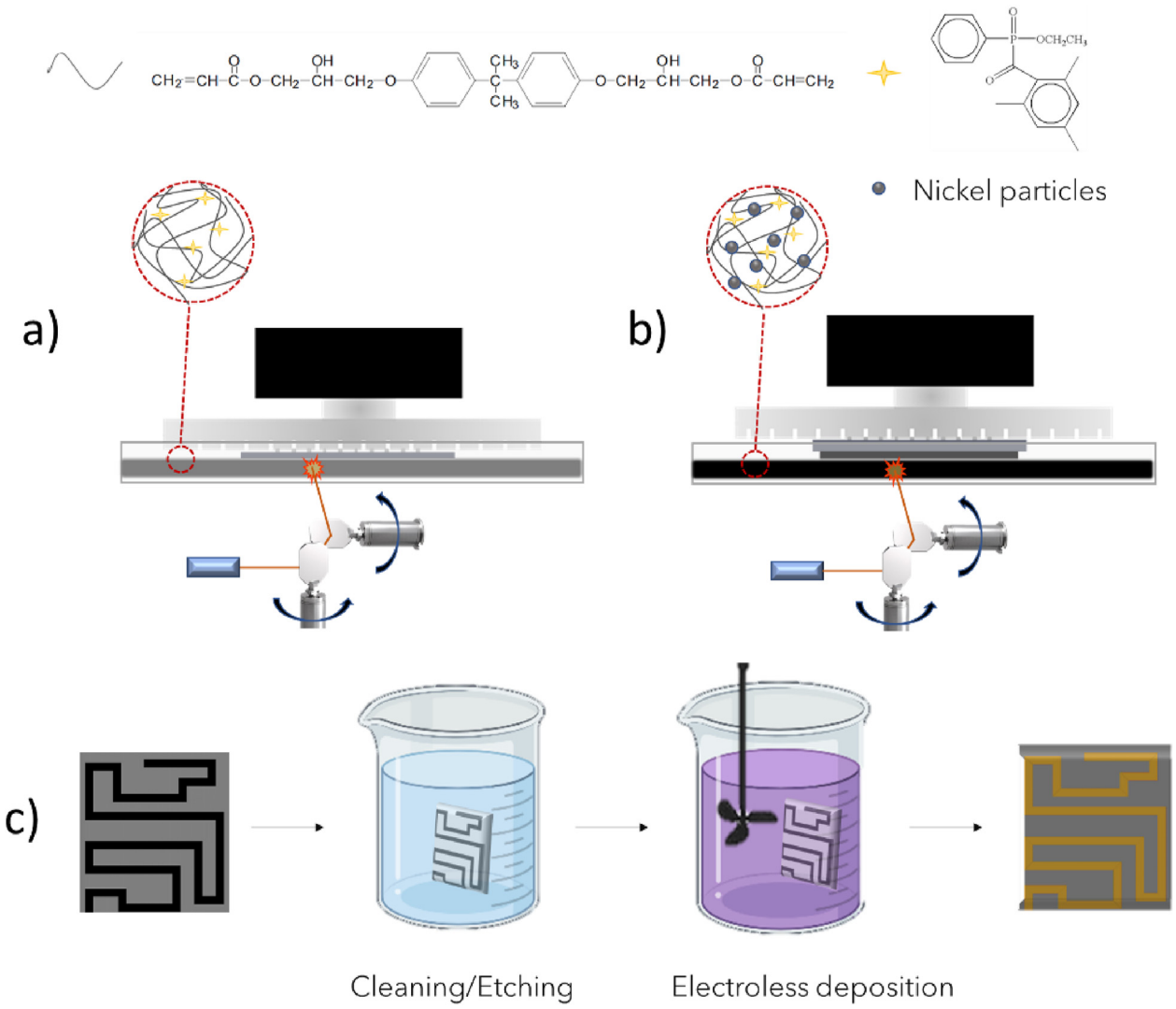

Fig. 1 – Schematic illustration of the straightforward process implemented to 3D print functional parts. Direct SLA-printing of photocurable structural polymer (a) and self-catalyzing Ni-loaded photopolymer (b). Selective metallization of 3D printed parts is achieved *via* standard electroless process avoiding the activation step (c).

formulations with lower particles content probably affecting the photo conversion of the polymer.

The solid residue above 460 °C substantially corresponded to the amount of Ni particles effectively present in the composite. Ni, indeed, melts at 1455 °C and it reasonably constituted the largest fraction of the solid phase present after the total degradation of the matrix. Residual values obtained are consistent with the nominal amount of Ni particles loaded in the formulations, which means that homogeneous inorganic fraction distribution within the polymer matrix was achieved.

The mechanical properties of the composites were determined performing Vickers microindentation tests and the resulting values of elastic modulus were correlated with the Ni content of the composites (obtained from the TGA). Fig. 4b shows the result obtained. Composition can be determined also performing EDS during SEM. EDS as analytical methodology, however, is characterized by an intrinsically limited spatial range, thus it gives information on the local Ni concentration in correspondence of a micrometric region of the sample, while TGA determines the Ni concentration for the whole analyzed sample. Fig. S4 reports the EDS compositional data obtained from the 10 % wt., 30 % wt. and 50 % wt. Ni samples. Considering the TGA data reported in Fig. 4b, for samples with loading up to 30% wt, the concentration of Ni nanoparticles actually presents in the composites after SLA printing, closely matched the expectable one (i.e., the nominal amount added to the resin). In the case of the 50 % wt. Ni sample, embedded Ni particles were significantly less than expected. This result suggests that the amount of Ni nanoparticles dispersed in the resin was probably excessive and it resulted in partial sedimentation during the printing process. Considering the EDS data, on the contrary, measured composition presented an irregular trend, which is indicative of localized variations in the Ni content at the microscale. Despite of this, the same general compositional trend identified with TGA data was observed also using EDS. As reported in Fig. 4b, the effect of the increasing Ni content on the elastic modulus is evident. Measured E increased from values equal

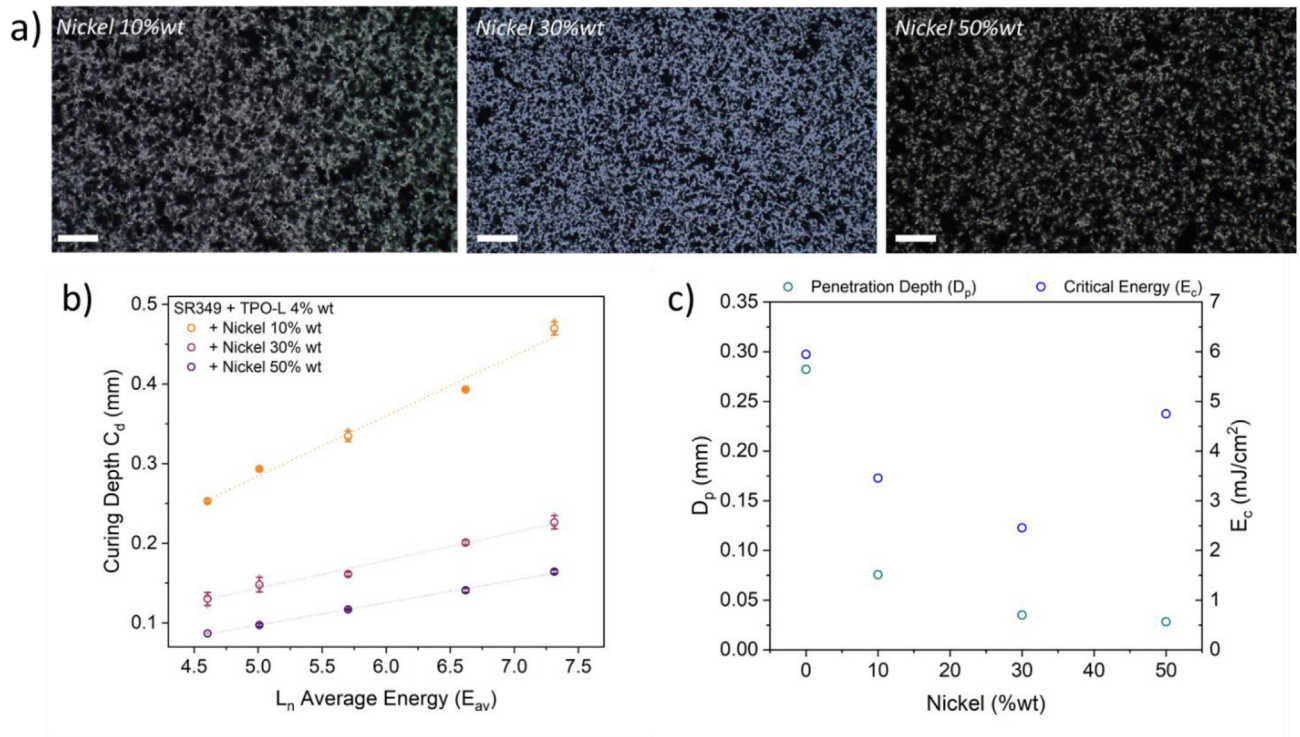

Fig. 2 – Optical microscopy (OM) images of metal-polymer samples photocured at increasing Ni loading (a). Scale bar is 50 μm. Laser working curves for the composites at increasing Ni loading were obtained by plotting experimental curing depths against the logarithm of average energy (b). Resulting penetration depth D_p was observed to decrease upon increasing with Ni content thus achieving higher SLA-printing resolution (c). Not significant differences were observed for the critical energy E_c.

to 4.01 ± 0.56 GPa (non-loaded resin) to maximum values of 14.77 ± 1.6 GPa for the 50 % wt. Ni resin.

The DSC analysis was performed for the neat and 30% wt. Ni-doped formulations (Fig. S5). The exothermal peak visible in the 100–200 °C range for Ni-doped sample show the presence of unreacted C=C bonds that complete their reactions upon increasing with the heat (no exothermal peaks were observed in the second heating scans – data not shown). Instead, no exothermic peak was observed in the pristine sample. This behavior is likely due to the large particles clusters, visible from SEM images, that could decrease the crosslink density of the polymer matrix and inhibit the complete cure of the photopolymer.

The phase composition of the composites was determined by performing XRD in Bragg-Brentano configuration. Fig. 4c shows the results obtained from the non-loaded SR349 resin and from the two composites containing 30 % wt. and 50 % wt. Ni. In general, the features visible at low angles (between 10° and 30°) can be associated to the photocured SR349 resin. Three peaks (at 14.2°, 17° and 25.5°) were found to superimpose to a broad peak centered around 20°. The latter is indicative of an amorphous phase, which coexists with some degree of crystallinity. Indeed, the three peaks originated from regularly spaced acrylate chains organized in a crystal lattice [46]. Being SR349 present in all the composites, the corresponding features were recorded for all the three sample. Their relative intensity, however, was considerably lower in the two Ni loaded samples due to the presence of the metal itself, which resulted prominent due to its high crystallinity. Ni peaks were found at 44.6° and 52° and were associated with the (111) and (200) crystallographic orientations of the fcc structure respectively. The Scherrer equation, evaluated using the full width at half maximum (FWHM) of the (111) peak, allowed to estimate a mean crystallite size of 56.8 nm for the Ni constituting the nanoparticles. This value, if compared with their mean diameter, suggests that the Ni nanoparticles here employed are characterized by a marked polycrystallinity.

Finally, the magnetic properties of the Ni loaded composites were determined. Fig. 4d reports the hysteresis cycle obtained from the 30 % wt. sample between −1 T and 1 T. At saturation, the composite exhibited a value of M_s equal to 15.82 emu g^{-1}. Considering that the concentration of metallic Ni was equal to 32 wt. % and that the SR349 matrix gave a negligible contribution to the magnetic behavior of the composite, the value of M_s for the Ni particles alone was estimated to be 49.44 emu/g. Given the polycrystalline nature of the particles employed, this value is reasonable if compared to what observed in literature for polycrystalline bulk Ni (e.g. 58.57 emu/g by Danan et al. [47]). From the coercivity point of view, the composite was characterized by a H_c value equal to 98 Oe (Fig. S6). This value is typical of soft magnetic materials but considerably higher than pure bulk Ni, which normally presents H_c values below 1 Oe [48,49]. Such high value of coercivity is justified by the fact that Ni is here present in the form of nanopowder. Ni, indeed, shows a high dependence

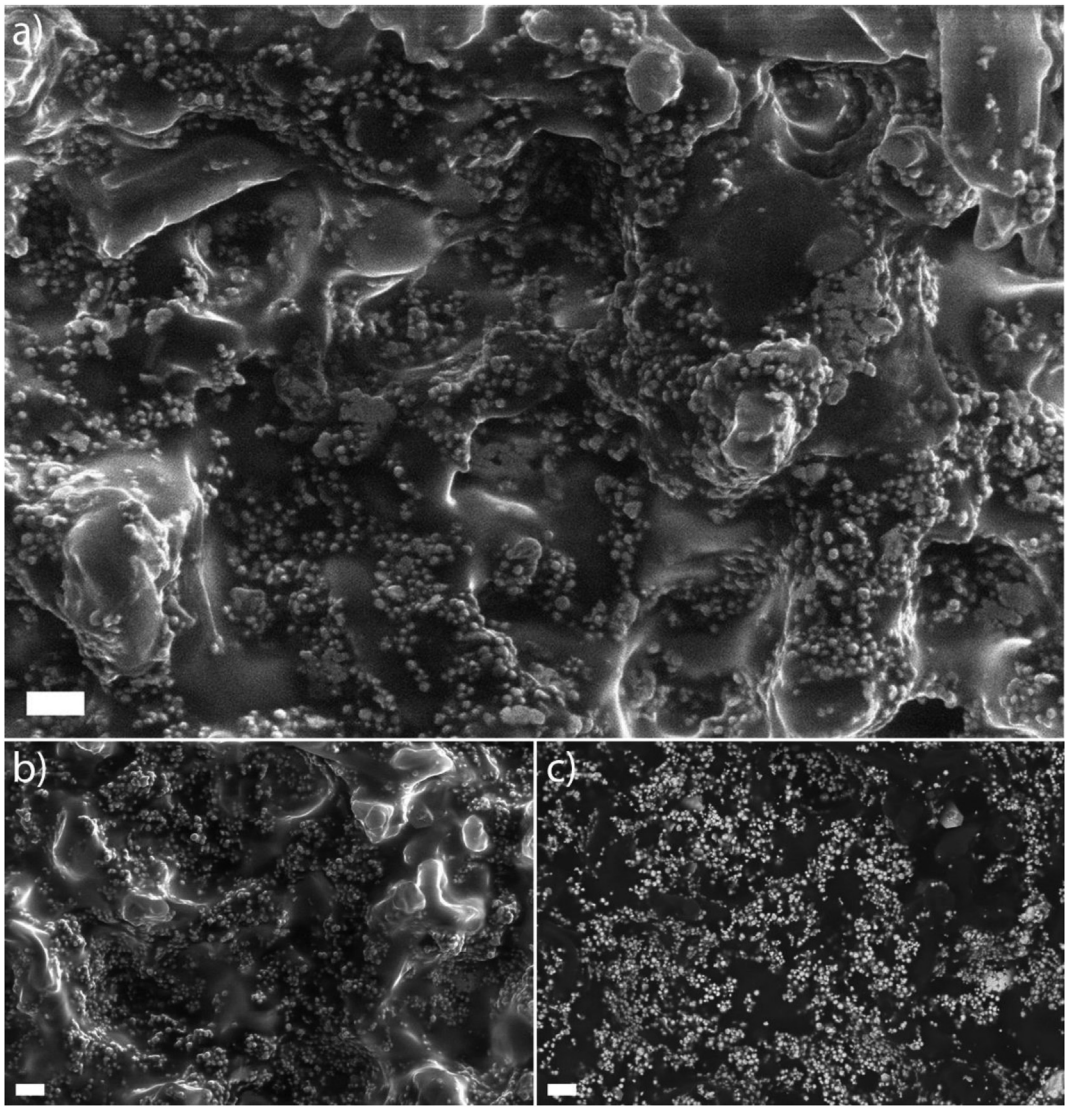

Fig. 3 – SEM micrograph of 30% (a) and 50% (b) wt. Ni loaded samples characterized by rough morphology. BS signal, which is characterized by an intrinsic chemical contrast, was acquired as well to better identify Ni nanoparticles and to show that quite homogeneous dispersion was achieved (c). All the scale bars visible in the figure correspond to 10 μm.

from morphology and phase structure for what concerns H_c. It is well-known that powder samples of Ni present values of coercivity in the 20–30 Oe range [49], while the same material can reach values of hundreds of Oe for H_c when in the form of nanowires [48]. Finally, remanence *Mr* was measured as well, resulting in a value of 6.7 emu g^{-1}.

3.3. *Selective electroless metallization*

Besides their intrinsic mechanical and magnetic properties, SLA printed SR349-Ni composites are characterized by another interesting property: the capacity to trigger autocatalytic electroless metal deposition. This property was verified attempting NiP electroless deposition on the surface of the test specimens. To understand the activation mechanism mediated by the Ni present in the composite, it is useful to recall the chemical reactions at the base of autocatalytic NiP plating [Eqs. (3)–(7)]

$$H_2PO_2^- \rightarrow HPO_2^- + [H] \quad (3)$$

$$Ni^{2+} + 2\,[H] \rightarrow Ni^0 + 2H^+ \quad (4)$$

$$H_2PO_2^- + 2\,H^+ + e^- \rightarrow 2H_2O + P \quad (5)$$

$$HPO_2^- + H_2O \rightarrow H_2PO_3^- + H^+ + e^- \quad (6)$$

$$2H^+ + 2\,e^- \rightarrow H_2 \quad (7)$$

Briefly, the active hydrogen coming from the decomposition of hypophosphite (Eq. (3)) reduces Ni^{2+} to metallic Ni (Eq. (4)). As a byproduct, the reaction also gives elemental P, which is incorporated in the final layer in the form of a solid solution (Eq. (5)). In addition, the reaction generates molecular hydrogen (Eqs. (6) and (7)), which evolves as gas bubbles. The

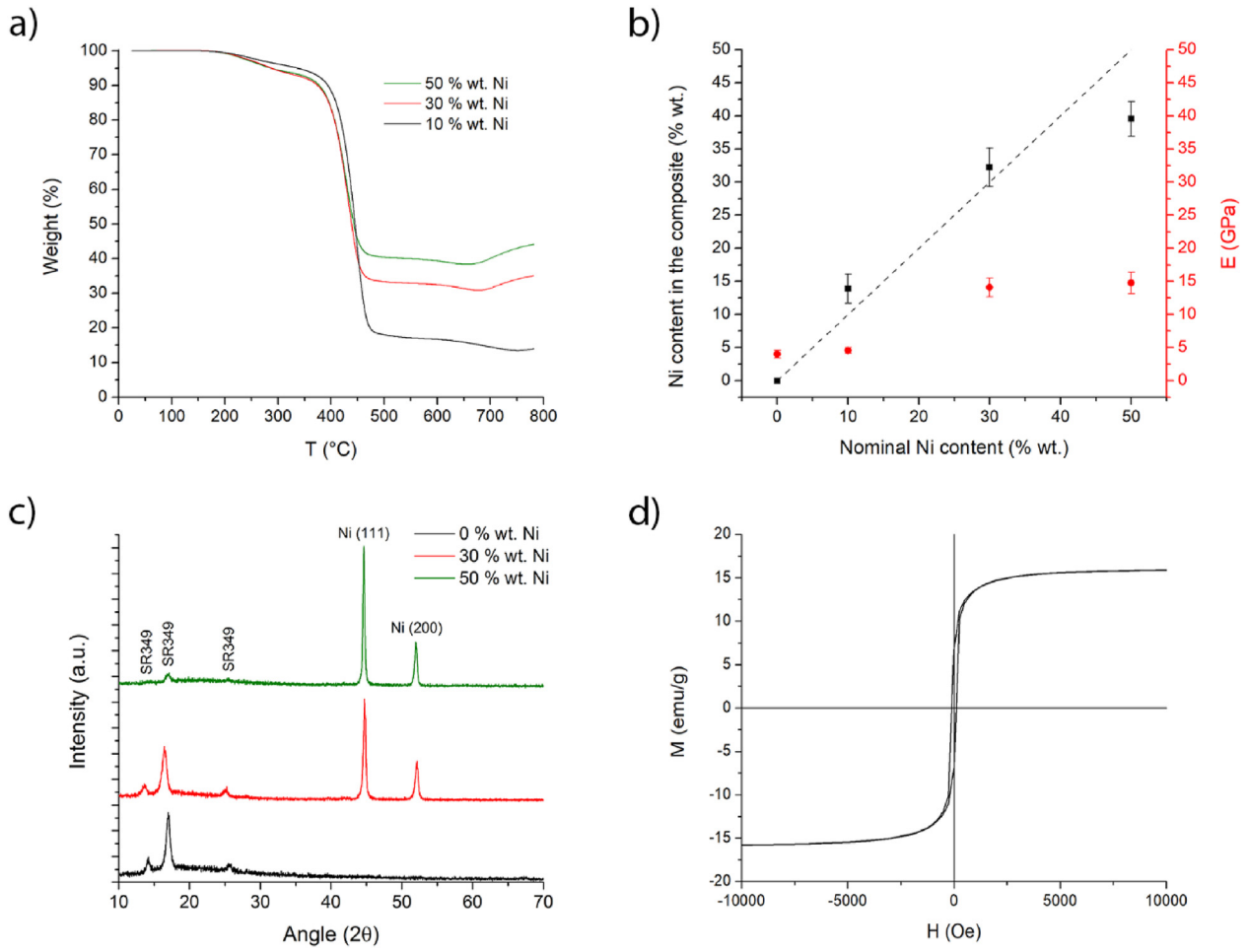

Fig. 4 – TGA analysis for the 10 % wt., 30 % wt. and 50 % wt. Ni composites (a). Nominal vs. experimental Ni content values for the composites, superimposed with the corresponding values of elastic modulus *E* (b). XRD characterization of the 30 % wt. and 50 % wt. Ni composites (c). Magnetic hysteresis curve of the 30 % wt. Ni composite (d).

critical step in the process is the decomposition of the hypophosphite ions, which is triggered by the presence of a catalytic surface. Normally, in the case of polymers, the surface is made catalytic by forming metallic Pd clusters on the surface via immersion in two separate aqueous solutions: one containing Pd^{2+} and the second containing a reducing agent [25,26]. In the case of the SR349-Ni composite, the catalytic material is represented by the Ni nanoparticles located in correspondence of the surface. These can start the electroless NiP deposition process without the need to activate the surface, conferring thus a self-activating character to the composite itself.

From the operative point of view, the surface was initially immersed in a KOH solution. In fact, the as printed composites presented the Ni nanoparticles located in correspondence of the surface in a non-optimal state. They were partially buried in the resin matrix and potentially covered by SR349 residues coming from the 3D printing step (Fig. 5a I). In order to expose and clean the particles, the test specimens were immersed in KOH, which attacked and partially dissolved the acrylate resin between the particles (Fig. 5a II). The immersion in KOH also increased the roughness of the surface, favoring thus metal adhesion due to mechanical interlocking [25]. The effect of KOH immersion (step II in Fig. 5a) is clearly visible in Fig. 5b and c, which describe the post-KOH morphology of the 30 % wt. and 50 % wt. Ni composites, respectively. The high roughness achieved at the end of the KOH treatment is particularly evident in Fig. 5b, while Fig. 3c clearly shows the Ni nanoparticles protruding from the resin matrix. At the end of the KOH immersion, the surface of the particles was quickly rinsed in diluted HCl to remove any trace of $Ni(OH)_2$ or NiO that possibly formed on the surface of the particles [50].

Once treated with HCl, the test specimens were immersed in a low temperature NiP electroless bath to deposit a continuous layer having a 1.5 μm nominal thickness (Fig. 5a III). As visible from Fig. 5d (30 % wt. Ni) and 3e (50 % wt. Ni), both composites successfully plated with a continuous and uniform layer of NiP (step III in Fig. 5a). Such coating was found to be highly adherent to the substrate and continuous all over the surface. Interestingly, a clear concentration dependent behavior for what concerns the capability of the composite to trigger a uniform electroless NiP deposition was observed. Samples printed at 10 % wt. Ni, for example, were unable to uniformly cover with metal. In some isolated spots

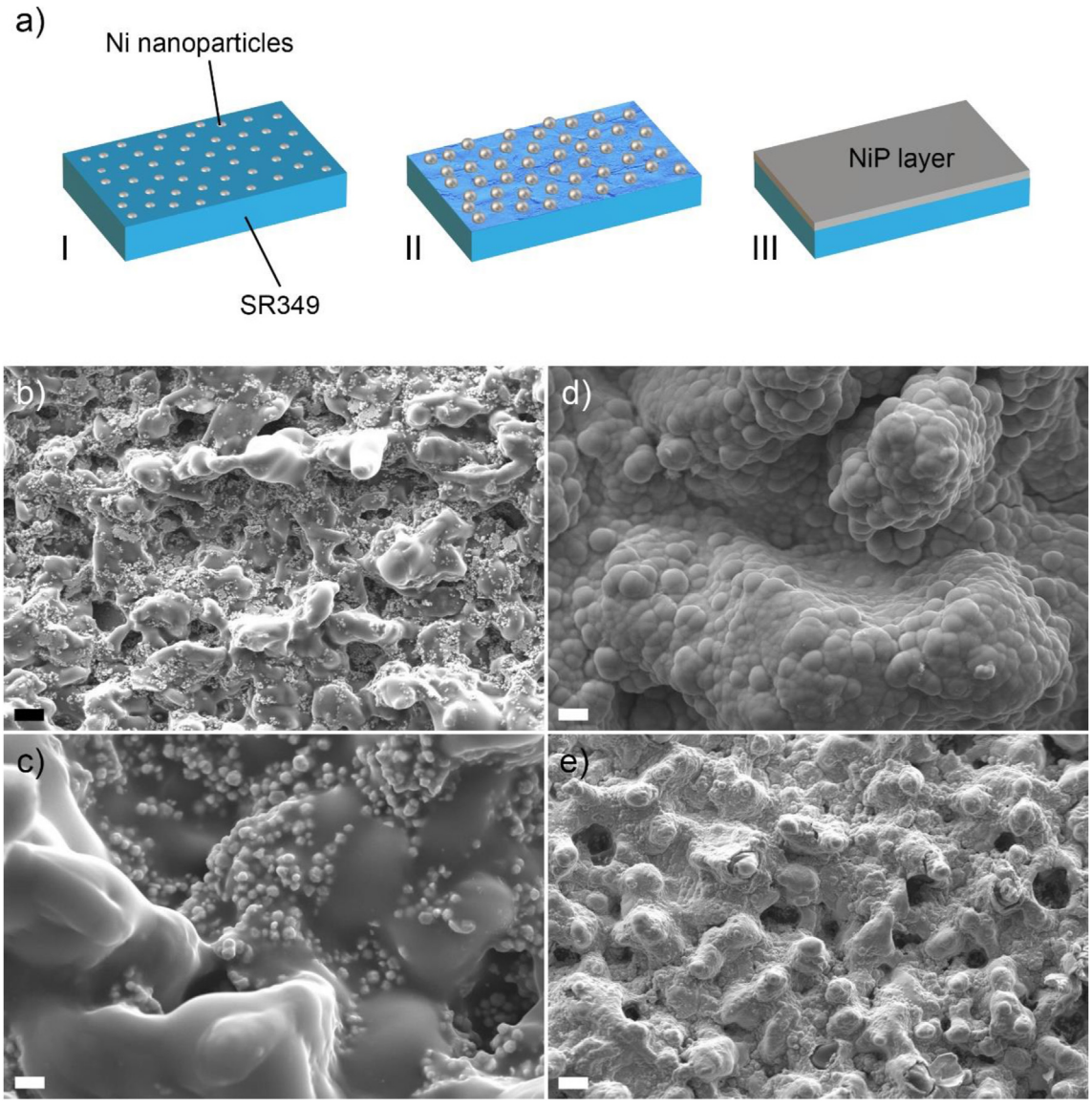

Fig. 5 – Schematic representation of the morphological transformations occurring on the surface of the SR349-Ni composite during the metallization process (a). SEM characterization of the 30 % wt. Ni composite after immersion in the KOH solution (b) and in the NiP electroless bath (d). SEM characterization of the 50 % wt. Ni composite after immersion in the KOH solution (c) and in the NiP electroless bath (e). Scale bars: 20 μm for (b), 4 μm for (c), 4 μm for (d) and 20 μm for (e).

on the samples, however, deposition started and nodular formations were observed on the surface of the composite (Fig. S7).

3.4. *Multimaterial 3D printing and selective metallization*

The self-activating behavior of the SR349-Ni composites presents an intrinsic interest for applications that combine a relevant magnetic behavior with a conductive surface. This can be the case of magnetic sensors or magnetically actuated switches [26]. However, when the goal is mere surface metallization, standard activation with Pd would be typically enough. The self-activating properties of the SR349-Ni composite can be exploited, on the contrary, to selectively metallize objects 3D printed using the multimaterial printing approach. It is possible to alternate non-loaded and Ni-loaded resins during SLA printing. By doing this, only regions printed with the loaded resin can metallize. This approach can be attractive for the realization of 3D printed electronics [51,52] and sensors [53], which typically require an alternance of conductive and non-conductive zones.

In this context, the demonstrator visible in Fig. 6a was created to demonstrate the possibility of selectively metallizing multimaterial SLA printed parts. Its square base was printed using non-loaded SR349 resin, which was later substituted, temporarily stopping the printing process, with the Ni-loaded composite. According to results obtained from the composite characterization and metalization, a resin loaded with Ni content higher than 10% wt., namely 30 % wt.,

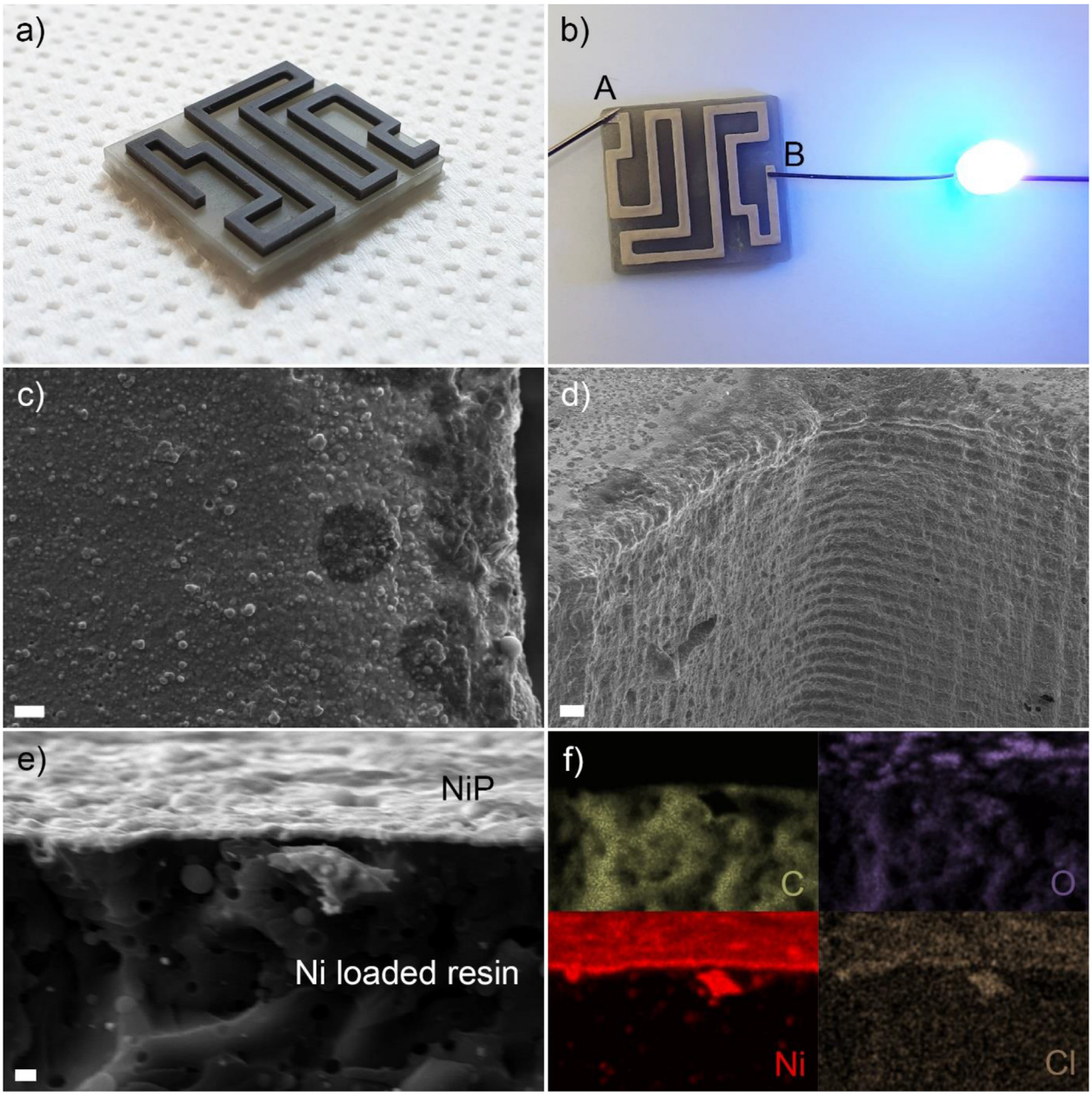

Fig. 6 – Picture of the as printed proof-of-concept demonstrator (a). Qualitative conductivity test performed on the selectively NiP metallized demonstrator (b). SEM characterization of the NiP metallized demonstrator (c and d). Cross-section of the NiP metallized demonstrator (e) and corresponding EDS elemental maps (f). Scale bars: 10 μm for (c), 20 μm for (d) and 2 μm for (e).

was exploited to print the intricate circuit visible on top of the square base. From the SLA manufacturing point of view, the multimaterial printing process was successful and yielded the result visible in Fig. 6a. As demonstrated by the cross-section reported in Fig. S8, no discontinuity could be detected at the interface between the loaded and the non-loaded resins. This resulted in a strong bonding between the two regions. The demonstrator was treated in KOH and metallized following the same methodology used for the test specimens. As a result, the surface of the demonstrator covered with NiP in correspondence of the circuit printed using the Ni-loaded resin (Fig. 6b). The NiP layer deposited on the circuit was found to be highly adherent and continuous, as demonstrated by its capability to close the circuit required to light a blue LED. In fact, the metallic layer easily sustained 15 mA of current, in front of a resistance equal to 3.1 Ω between the two points A and B in Fig. 6b.

Fig. 6c reports the morphology observed via SEM in correspondence of the upper face of the circuit and on one of the edges. Apparently, the Ni uniformly covered the entire surface, forming a compact layer. The zone depicted in Fig. 6d presents a characteristic step-like morphology, which is a result of the layer-by-layer material deposition typical of SLA printing process. Fig. 6e depicts a section of the demonstrator,

while Fig. 6f reports the corresponding EDS mapping for C, O, Ni and Cl. The composite resulted covered by a 940 ± 74 nm thick layer of NiP. The expected thickness of the NiP layer, considering bath temperature and immersion time [26], was 1.5 μm. This discrepancy suggests that probably the initial phase of the deposition, following activation by the Ni particles embedded in the composite, yielded a highly non-linear increase of thickness. From the compositional point of view, the EDS elemental maps reported in Fig. 6f clearly visualize the distribution of the elements in the cross-section, with C relegated to the resin matrix of the composite and Ni concentrated in the NiP layer. Some Ni, however, was obviously present also in the matrix in the form of Ni nanoparticles. EDS maps for O are characterized by detectable amounts of the element both in the resin matrix (being an acrylate) and in the NiP layer (probably as a consequence of oxidation). Interestingly, also the presence of detectable amounts of Cl was observed. Cl contamination is a natural consequence of the use of a Cl-rich electrolyte for the deposition of NiP.

4. Conclusions

In conclusion, we reported a successful straightforward and low-cost 3D printed method for stereolithography (SLA)-printing of multifunctional parts directly embedded in structural parts. To this end, a novel self-catalysing metal-photopolymer composites was formulated by doping acrylates-based resin with Ni particles able to trigger metal deposition by electroless deposition. The Ni content was optimized to guarantee high-resolution SLA-printing of self-activating structures as well as to guarantee homogeneous deposition of a continuous metal layer. The SLA high-resolution processability of the composites at higher Ni content was attested by the values of penetration depth and critical energies obtained. The addition of Ni nanoparticles considerably increased the elastic modulus of the printed material (up to roughly 370% of the value recorded for the non-loaded material). Finally, we demonstrated the capability of Ni-doped composite to trigger electroless deposition of homogeneous NiP compact layers even when working at low temperature alkaline bath conditions. A concentration dependent behavior was observed: when Ni nanoparticles were present in a sufficient amount, they successfully triggered NiP electroless deposition. The effect of NiP deposition as a function of Ni-loading suggested that 30%wt of Ni as the optimal condition to efficiently start NiP deposition. A lower Ni content resulted in a surface covered by small isolated NiP nodules. This happened in the case of the 10 % wt. Ni sample. To evaluate the feasibility of selective metallization, a bulk demonstrator constituted by both non-loaded and Ni-loaded parts was manufactured using the multimaterial SLA printing approach. Upon immersion in the electroless NiP bath, metallization successfully occurred only in correspondence of the Ni loaded pattern printed, whereas non-loaded regions did not metallize. The characterization carried out evidenced the formation of a continuous conductive coating on the surface. This result suggests that multilayer structures, obtained thanks to a smart alternance of self-activating and non-activating materials, can be potentially manufactured. Upon selective metallization, these structures would present controlled paths for electric conduction and may find application in the manufacturing of 3D printed multilayered electronic circuits or of sensors combining magnetic and conductive properties.

Declaration of competing interest

The authors declare that they have no known competing financial interests or personal relationships that could have appeared to influence the work reported in this paper.

Appendix A. Supplementary data

Supplementary data to this article can be found online at https://doi.org/10.1016/j.jmrt.2022.12.035.

REFERENCES

[1] Vaezi M, Seitz H, Yang S. A review on 3D micro-additive manufacturing technologies. Int J Adv Manuf Technol 2013;67:1721–54.
[2] Chen L, He Y, Yang Y, Niu S, Ren H. The research status and development trend of additive manufacturing technology. Int J Adv Manuf Technol 2017;89:3651–60.
[3] Gibson I, Rosen DW, Stucker B, Khorasani M. Additive manufacturing technologies, vol. 17. Springer; 2021.
[4] Huber C, Abert C, Bruckner F, Groenefeld M, Muthsam O, Schuschnigg S, et al. 3D print of polymer bonded rare-earth magnets, and 3D magnetic field scanning with an end-user 3D printer. Appl Phys Lett 2016;109:162401.
[5] Dong Y, Bao C, Kim WS. Sustainable additive manufacturing of printed circuit boards. Joule 2018;2:579–82.
[6] Postiglione G, Natale G, Griffini G, Levi M, Turri S. Conductive 3D microstructures by direct 3D printing of polymer/carbon nanotube nanocomposites via liquid deposition modeling. Composites Part A Appl Sci Manuf 2015;76:110–4.
[7] Lopes AJ, Lee IH, Macdonald E, Quintana R, Wicker R. Laser curing of silver-based conductive inks for in situ 3D structural electronics fabrication in stereolithography. J Mater Process Technol 2014;214:1935–45. https://doi.org/10.1016/j.jmatprotec.2014.04.009.
[8] Wang X, Jiang M, Zhou Z, Gou J, Hui D. 3D printing of polymer matrix composites: a review and prospective. Compos B Eng 2017;110:442–58.
[9] Pervaiz S, Qureshi TA, Kashwani G, Kannan S. 3D printing of fiber-reinforced plastic composites using fused deposition modeling: a status review. Materials (Basel) 2021;14:4520.
[10] Baker DV, Bao C, Kim WS. Highly conductive 3D printable materials for 3D structural electronics. ACS Appl Electron Mater 2021;3:2423–33.
[11] Lazarus N, Tsang HH. 3-D printing structural electronics with conductive filaments. IEEE Trans Compon Packag Manuf Technol 2020;10:1965–72.
[12] Niendorf K, Raeymaekers B. Additive manufacturing of polymer matrix composite materials with aligned or organized filler material: a review. Adv Eng Mater 2021;23:2001002.
[13] Xu W, Jambhulkar S, Ravichandran D, Zhu Y, Kakarla M, Nian Q, et al. 3D printing-enabled nanoparticle alignment: a review of mechanisms and applications. Small 2021;17:2100817.

[14] Compton BG, Lewis JA. 3D-printing of lightweight cellular composites. Adv Mater 2014;26:5930–5.
[15] Greenhall J, Raeymaekers B. 3D Printing macroscale engineered materials using ultrasound directed self-assembly and stereolithography. Adv Mater Technol 2017;2:1700122.
[16] Niendorf K, Raeymaekers B. Combining ultrasound directed self-assembly and stereolithography to fabricate engineered polymer matrix composite materials with anisotropic electrical conductivity. Compos B Eng 2021;223:109096.
[17] Yang Y, Chen Z, Song X, Zhu B, Hsiai T, Wu P-I, et al. Three dimensional printing of high dielectric capacitor using projection based stereolithography method. Nano Energy 2016;22:414–21.
[18] Xue J, Gao L, Hu X, Cao K, Zhou W, Wang W, et al. Stereolithographic 3D printing-based hierarchically cellular lattices for high-performance quasi-solid supercapacitor. Nano-Micro Lett 2019;11:1–13.
[19] Djokic Stojan S, Cavalloti PL. Electroless deposition: theory and practice, vol. 48; 2010. https://doi.org/10.1007/978-1-4419-5589-0.
[20] Choi JW, Kim HC, Wicker R. Multi-material stereolithography. J Mater Process Technol 2011;211:318–28. https://doi.org/10.1016/j.jmatprotec.2010.10.003.
[21] Zhang J, Feng J, Jia L, Zhang H, Zhang G, Sun S, et al. Laser-induced selective metallization on polymer substrates using organocopper for portable electronics. ACS Appl Mater Interfaces 2019;11:13714–23. https://doi.org/10.1021/acsami.9b01856.
[22] Palazzi V, Su W, Bahr R, Bittolo-Bon S, Alimenti F, Mezzanotte P, et al. 3-D-Printing-Based selective-ink-deposition technique enabling complex antenna and RF structures for 5G applications up to 6 GHz. IEEE Trans Compon Packag Manuf Technol 2019;9:1434–47. https://doi.org/10.1109/TCPMT.2019.2919187.
[23] Zega V, Invernizzi M, Bernasconi R, Cuneo F, Langfelder G, Magagnin L, et al. The first 3D-printed and wet-metallized three-axis accelerometer with differential capacitive sensing. IEEE Sensor J 2019;19:9131–8.
[24] Xu J, Wu D, Hanada Y, Chen C, Wu S, Cheng Y, et al. Electrofluidics fabricated by space-selective metallization in glass microfluidic structures using femtosecond laser direct writing. Lab Chip 2013;13:4608–16. https://doi.org/10.1039/c3lc50962a.
[25] Bernasconi R, Natale G, Levi M, Magagnin L. Electroless plating of NiP and Cu on polylactic acid and polyethylene terephthalate glycol-modified for 3D printed flexible substrates. J Electrochem Soc 2016;163:D526–31.
[26] Bernasconi R, Credi C, Tironi M, Levi M, Magagnin L. Electroless metallization of stereolithographic photocurable resins for 3D printing of functional microdevices. J Electrochem Soc 2017;164:B3059–66. https://doi.org/10.1149/2.0081705jes.
[27] Li J, Wang Y, Xiang G, Liu H, He J. Hybrid additive manufacturing method for selective plating of freeform circuitry on 3D printed plastic structure. Adv Mater Technol 2019;4:1800529.
[28] Chen JJ, Guo YL, Wang Y, Zhang J, Li HJ, Feng ZS. Selective metallization of alumina ceramics by inkjet printing combined with electroless copper plating. J Mater Chem C 2016;4:10240–5. https://doi.org/10.1039/c6tc03315f.
[29] Ryspayeva A, Jones TDA, Khan SR, Esfahani MN, Shuttleworth MP, Harris RA, et al. Selective metallization of 3D printable thermoplastic polyurethanes. IEEE Access 2019;7:104947–55. https://doi.org/10.1109/ACCESS.2019.2931594.
[30] Zhang J, Zhou T, Wen L, Zhang A. Fabricating metallic circuit patterns on polymer substrates through laser and selective metallization. ACS Appl Mater Interfaces 2016;8:33999–4007. https://doi.org/10.1021/acsami.6b11305.
[31] Xu H, Zhang J, Feng J, Zhou T. Fabrication of copper patterns on polydimethylsiloxane through laser-induced selective metallization. Ind Eng Chem Res 2021;60:8821–8. https://doi.org/10.1021/acs.iecr.1c01668.
[32] Rytlewski P, Jagodziński B, Karasiewicz T, Augustyn P, Kaczor D, Malinowski R, et al. Copper filled poly (Acrylonitrile-co-Butadiene-co-Styrene) composites for laser-assisted selective metallization. Materials (Basel) 2020;13:2224.
[33] Li J, Zhang Y, Wang P, Wang G, Liu Y, Liu Y, et al. Selectively metalizable stereolithography resin for three-dimensional DC and high-frequency electronics via hybrid additive manufacturing. ACS Appl Mater Interfaces 2021;13:22891–901. https://doi.org/10.1021/acsami.1c01199.
[34] Lee D, Kim BY, Park CH, Jeong G, Park SD, Yoo MJ, et al. Photocurable three-dimensional printing resin to enable laser-assisted selective electroless metallization for customized electronics. ACS Appl Polym Mater 2021;3:4735–45. https://doi.org/10.1021/acsapm.1c00997.
[35] Taormina G, Sciancalepore C, Bondioli F, Messori M. Special resins for stereolithography: in situ generation of silver nanoparticles. Polymers (Basel) 2018;10. https://doi.org/10.3390/polym10020212.
[36] Ha CW, Prabhakaran P, Son Y. 3D-printed polymer/metal hybrid microstructures with ultraprecision for 3D microcoils. 3D Print Addit Manuf 2019;6:165–70. https://doi.org/10.1089/3dp.2018.0139.
[37] Jammes A, Petisme M, Staelens K. Metallization and selective metallization of silver by spraying. Surf Coating Technol 2017;332:560–3. https://doi.org/10.1016/j.surfcoat.2017.10.051.
[38] Lee S, Wajahat M, Kim JH, Pyo J, Chang WS, Cho SH, et al. Electroless deposition-assisted 3D printing of micro circuitries for structural electronics. ACS Appl Mater Interfaces 2019;11:7123–30. https://doi.org/10.1021/acsami.8b18199.
[39] Zhan J, Tamura T, Li X, Ma Z, Sone M, Yoshino M, et al. Metal-plastic hybrid 3D printing using catalyst-loaded filament and electroless plating. Addit Manuf 2020;36:101556. https://doi.org/10.1016/j.addma.2020.101556.
[40] Lazarus N, Bedair SS, Hawasli SH, Kim MJ, Wiley BJ, Smith GL. Selective electroplating for 3D-printed electronics. Adv Mater Technol 2019;4:1–5. https://doi.org/10.1002/admt.201900126.
[41] Laureto J, Tomasi J, King JA, Pearce JM. Thermal properties of 3-D printed polylactic acid-metal composites. Prog Addit Manuf 2017;2:57–71. https://doi.org/10.1007/s40964-017-0019-x.
[42] Pigliaru L, Rinaldi M, Ciccacci L, Norman A, Rohr T, Ghidini T, et al. 3D printing of high performance polymer-bonded PEEK-NdFeB magnetic composite materials. Funct Compos Mater 2020;1:1–17. https://doi.org/10.1186/s42252-020-00006-w.
[43] Jacobs PF. Rapid prototyping & manufacturing: fundamentals of stereolithography. Society of Manufacturing Engineers; 1992.
[44] Credi C, Levi M, Turri S, Simeone G. Stereolithography of perfluoropolyethers for the microfabrication of robust omniphobic surfaces. Appl Surf Sci 2017;404:268–75.
[45] Credi C, Fiorese A, Tironi M, Bernasconi R, Magagnin L, Levi M, et al. 3D printing of cantilever-type microstructures by stereolithography of ferromagnetic photopolymers. ACS Appl Mater Interfaces 2016;8:26332–42.
[46] Patil DM, Phalak GA, Mhaske ST. Design and synthesis of bio-based UV curable PU acrylate resin from itaconic acid for coating applications. Des Monomers Polym 2017;20:269–82. https://doi.org/10.1080/15685551.2016.1231045.

[47] Danan H, Herr A, Meyer AJP. New determinations of the saturation magnetization of nickel and iron. J Appl Phys 1968;39:669–70. https://doi.org/10.1063/1.2163571.
[48] Choudhury PK, Banerjee S, Ramaprabhu S, Ramesh KP, Menon R. Variations in magnetic properties of nanostructured nickel. J Nanosci Nanotechnol 2013;13:8162–6. https://doi.org/10.1166/jnn.2013.7931.
[49] Kisker H, Gessmann T, Wurschum R, Kronmüller H, Schaefer HE. Magnetic properties of high purity nanocrystalline nickel. Nanostruct Mater 1995;6:925–8. https://doi.org/10.1016/0965-9773(95)00211-1.
[50] Medway SL, Lucas CA, Kowal A, Nichols RJ, Johnson D. In situ studies of the oxidation of nickel electrodes in alkaline solution. J Electroanal Chem 2006;587:172–81.
[51] Nassar H, Dahiya R. Fused deposition modeling-based 3D-printed electrical interconnects and circuits. Adv Intell Syst 2021;3:2100102.
[52] Espera AH, Dizon JRC, Chen Q, Advincula RC. 3D-printing and advanced manufacturing for electronics. Prog Addit Manuf 2019;4:245–67.
[53] Khosravani MR, Reinicke T. 3D-printed sensors: current progress and future challenges. Sensors Actuators A Phys 2020;305:111916.